Journal of the Geological Society, London, Vol. **165**, 2008, pp. 467–478. Printed in Great Britain.

Variscan evolution of the Tanneron massif, SE France, examined through U–Pb monazite ages

ANTOINE DEMOUX[1], URS SCHÄRER[2] & MICHEL CORSINI[2]

[1]*Institut für Geowissenschaften, Johannes Gutenberg Universität, Becherweg 21, 55099 Mainz, Germany (e-mail: demoux@uni-mainz.de)*

[2]*Géosciences Azur (UMR 6526), Université de Nice Sophia–Antipolis, Parc Valrose, F-06108 Nice Cedex 2, France*

Abstract: The Tanneron massif belongs to the southernmost segment of the Variscan belt in France and is composed of migmatitic orthogneisses and paragneisses cross-cut by a main tonalite–granite complex. Late Carboniferous detrital basins are bounded by north–south-trending ductile to brittle normal faults and delineate three distinct zones. Our new isotope dilution U–Pb monazite dating indicates a pre-Variscan history in the central part of the massif recorded by monazites from an orthogneiss yielding ages from 440 to 410 Ma, whereas monazites from a migmatitic paragneiss record a late Carboniferous high-*T* event at 317 ± 1 Ma. In the eastern part, a migmatization event is recorded by monazites from a synkinematic leucogranitic layer and a mylonitic orthogneiss yielding ages of 309 ± 5 and 310 ± 2 Ma, respectively. Later post-collisional magmatism related to lithospheric thinning is recorded by the intrusion of undeformed granitic bodies at 302 ± 4 and 297 ± 5 Ma, and marks the final stage of the Variscan evolution. The data indicate the presence of two crustal blocks, displaying different levels of exposure of the Variscan crust. The overall tectonomagmatic evolution of this massif suggests a strong affinity with the internal part of the Variscan belt.

Exhumed segments of deeply eroded orogenic belts can be used to study space–time relationships between deformation, metamorphism and crustal melting in deep and shallow crustal levels, with the purpose of constraining the geodynamic evolution of complex collision zones, such as the Variscan belt.

The Variscan belt of western Europe results from the collision between two major continents, Gondwana to the south and Laurussia–Baltica to the north, and several micro-continental blocks such as Avalonia and Armorica, from middle Devonian to middle Carboniferous time (e.g. Matte 2001). The evolution of this orogenic system is characterized by a high-*P*–low-*T* metamorphism related to an early subduction stage (Lardeaux *et al*. 2001). The collisional stage (middle Carboniferous) is marked by nappe stacking under medium- to high-grade metamorphism coeval with the intrusion of granitoid bodies. Finally, the late to post-orogenic re-equilibration of the thickened crust is associated with widespread high-*T*–low-*P* metamorphism and significant melting of the crust (Gardien *et al*. 1997).

Located in SE France (Fig. 1), the Tanneron massif was chosen to constrain the timing of the high-*T* regime because (1) it exposes an almost complete section through fresh rocks and (2) few petrological and geochronological data are available on high-*T* metamorphism, crustal melting and magmatism. In the present paper we focus on isotope dilution thermal ionization mass spectrometry (ID-TIMS) U–Pb dating on monazite ($Ce,La(PO_4)$), which is a high-*T* accessory phase forming either in metamorphic rocks under upper amphibolite and anatectic metamorphic conditions and/or in peraluminous melts and large granitic bodies (Schärer & Allègre 1983; Williams 2001). The interpretation of monazite ages from high-grade gneiss terranes is often difficult, because monazite grains may contain distinct compositional domains, usually interpreted in terms of different generations of growth (e.g. Williams *et al*. 2006) and/or may have been affected by later alteration processes. Therefore, for each monazite population the internal structure of the grains was characterized by back-scattered electron (BSE) images to better constrain the significance of the monazite U–Pb results.

Geological setting

The Crystalline Provence

Exposed along the Mediterranean Sea, the Maures–Tanneron massif forms part of the Crystalline Provence (Fig. 1a), which constitutes one of the southernmost segments of the Variscan belt in France (Matte 2001).

The Crystalline Provence consists of low- to high-grade metamorphic rocks intruded by Carboniferous granitoids and overlain by late Carboniferous coal basins (e.g. Crévola & Pupin 1994). The Tanneron massif to the north (study area) is separated from the Maures massif to the south by an east–west-trending Permian basin (Fig. 1b). Both massifs are cross-cut by three main north–south-trending faults (the Grimaud fault in the Maures massif, the Joyeuse and La Moure faults in the Tanneron massif). Late Carboniferous unmetamorphosed continental detrital basins are preserved adjacent to these faults (the Plan-de-la-Tour basin in the Maures massif, the Pennafort and Reyran basins in the Tanneron massif). Both massifs seem to have experienced the same thermal and structural history, as shown by similarities in their lithological, tectonic and metamorphic features (Toutin-Morin *et al*. 1994). The western metamorphic unit (Fig. 1b) comprises Lower Palaeozoic metasediments of low metamorphic grade. The central metamorphic unit consists of the Bormes orthogneiss, paragneisses and aluminous micaschists. The La Gardes–Freinet sequence is a tectonic mélange of high metamorphic grade including lenses of a bimodal association (leptyno-amphibolitic complex) embedded in slightly migmatitic gneisses. This sequence contains high-pressure relicts (garnet–spinel peridotite, Bouloton *et al*. 1998; coronitic metagabbros, Seyler 1982) that have not been precisely dated. The eastern metamorphic unit, east of the Grimaud and Joyeuse faults (Fig.

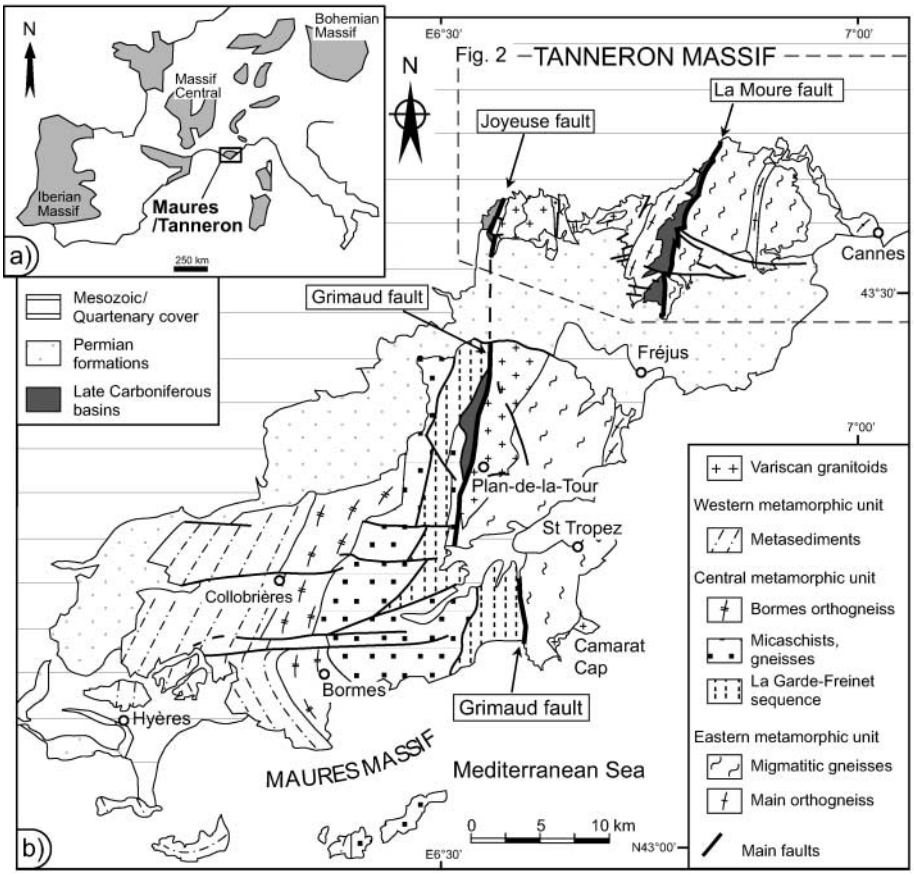

Fig. 1. (**a**) Distribution of main Variscan basements (grey) in western Europe and location of the study area. (**b**) Simplified geological sketch map of the Tanneron and Maures massifs (modified after Crévola & Pupin 1994). The dashed rectangle (Fig. 2) indicates the study area.

1b), is mainly composed of migmatitic orthogneisses and paragneisses that contain locally amphibolitized eclogitic lenses (e.g. Crévola *et al*. 1991). The Plan-de-la-Tour–Rouet magmatic complex is bordered to the west by the north–south-trending polyphase Grimaud–Joyeuse fault, which separates the central and eastern units.

The bulk geometry of the Maures and Tanneron massifs results from a polyphase tectonometamorphic history inferred from superimposed and various metamorphic fabrics, foliations and lineations (Bellot 2005, and references therein). The first phases of deformation (D_1 and D_2) are characterized by isoclinal and sheaths folds with S_1–S_2 axial planar foliation and L_1–L_2 stretching lineation associated with MP–MT metamorphism and partial melting. These early episodes of ductile deformation are related to nappe stacking during crustal collision. The last phases of deformation (D_3 and D_4) correspond to the development of north–south-trending strike-slip shear zones combined with the formation of kilometre-scale upright folds, Late Carboniferous intracontinental basins, LP–HT metamorphism and late tectonic magmatism. These late episodes correspond to orogen-parallel shearing in a transpressional regime associated with thermal re-equilibration of the lower crust during the post-collision stage.

The Tanneron massif

The present study focuses on the Tanneron massif, which covers an area of about 40 km × 15 km (Fig. 2a). The massif can be divided into three domains separated by major north–south-trending faults; namely, the La Moure and Joyeuse faults (Fig. 2b). At the scale of the massif, the metamorphic rocks display a penetrative foliation with a stretching and mineral lineation related to the D_2 deformational phase. This rock fabric is overprinted by an axial planar S_3 crenulation–schistosity of kilometre-scale synform and antiform folds (Fig. 2b), associated with the D_3 event. The eastern domain, west of the La Moure fault (Fig. 2a), is composed of a wide migmatitic augengneiss, a thick series of migmatitic paragneisses with micaschists equilibrated under biotite–muscovite–sillimanite–garnet metamorphic conditions, and scarce amphibolite lenses with eclogitic relicts (e.g. Crévola & Pupin 1994). Intercalated with these series is a mylonitic orthogneiss, affected by a roughly north–south-trending dextral high-*T* ductile shear zone. This orthogneiss contains locally preserved igneous textures of monzonitic composition including garnet and cordierite (Crévola & Pupin 1994). The central domain is limited to the west by the Joyeuse fault and to the east by the La Moure fault and the late Carboniferous Reyran basin (Fig. 2a). The basement to this coal basin is composed of a wide and homogeneous orthogneiss formation. Adjacent to this orthogneiss is a thick sequence of orthogneisses and paragneisses affected by progressive partial melting from east to west. Westward, this sequence is characterized by the occurrence of strongly migmatitic sillimanite-bearing gneisses showing occasionally the presence of cordierite. This series is intruded by an east–west-trending tourmaline-bearing leucogranitic body associated with a swarm of leucogranitic dykes that are either parallel or oblique to the surrounding composite foliation. To the west, the migmatitic gneisses are intruded by a tonalitic and granitic complex (Rouet magmatic complex) bounded along its western flank by the Joyeuse fault. To the west of the Joyeuse fault (Fig. 2a), the western domain is composed of a narrow band of migmatitic paragneisses and micaschists forming the basement to the small Late Carboniferous Pennafort coal basin.

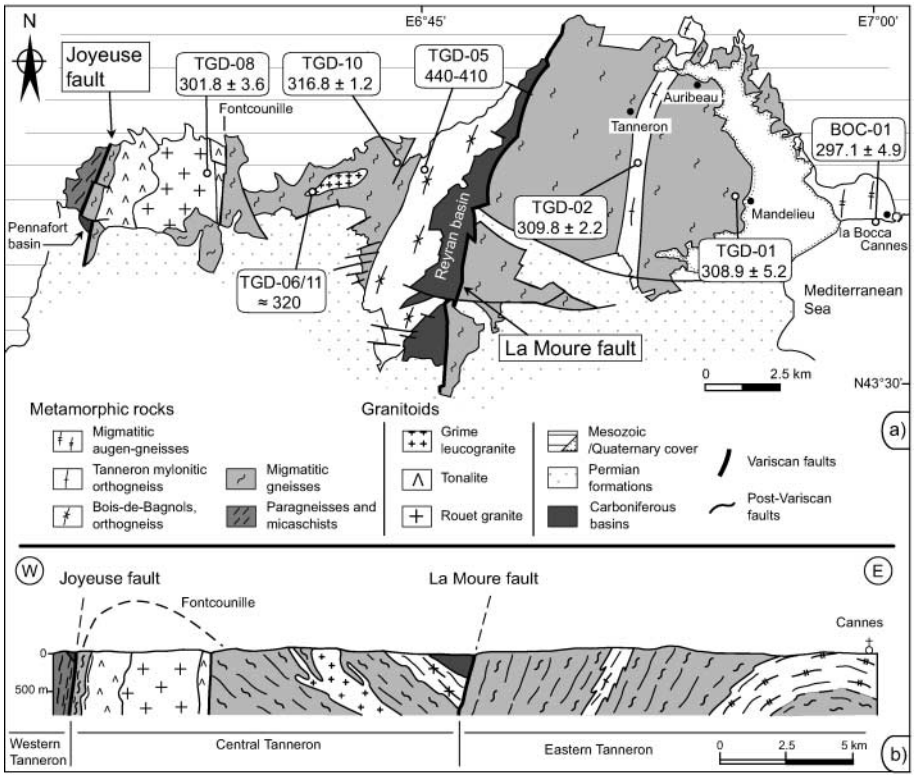

Fig. 2. (**a**) Geological sketch map and (**b**) schematic cross-section of the Tanneron massif (adapted from Crévola *et al*. 1991), showing the major lithotectonic units and the location of the analysed samples. U–Pb monazite ages are from this study and given in million years with error at 2σ level.

Previous geochronological data

The Maures massif

In the central metamorphic unit (Fig. 1b) Rb–Sr whole-rock ages (Maluski & Allègre 1970) and ^{40}Ar–^{39}Ar ages on biotite (Maluski & Gueirard 1978) record, for the Bormes orthogneiss protoliths, intrusion ages between 630 and 550 Ma. In the leptyno-amphibolitic complex Innocent *et al*. (2003) reported a U–Pb zircon age of 548 +15/−7 Ma from a felsic volcanic rock. This age is interpreted as the age of a bimodal magmatism related to a Pre-Variscan extensional setting along the north Gondwana margin. A U–Pb monazite age of 345 ± 3 Ma (Bormes orthogneiss, Moussavou 1998) and a whole-rock Rb–Sr age of 348 ± 7 Ma (amphibolite from the leptyno-amphibolitic complex, Innocent *et al*. 2003) are interpreted as the age of the regional metamorphism under amphibolite-facies conditions. This event is coeval with a heterogeneous ductile deformation related to a top-to-the-north sense of shear (Vauchez & Bufalo 1988). In the eastern metamorphic unit, U–Pb dating on monazite yields an age of 331 ± 3 Ma (Moussavou 1998) interpreted as the time of migmatization.

An initial stage of calc-alkaline magmatism is recorded by zircon U–Pb ages of 338 ± 6 Ma (Hermitan granite, central metamorphic unit) and 334 ± 3 Ma (Reverdit tonalite eastern metamorphic unit; Moussavou 1998). A second intrusive event is recorded in the eastern metamorphic unit by the Plan-de-la-Tour granite, which has yielded Rb–Sr whole-rock isochron emplacement ages between 334 ± 10 Ma (Roubault *et al*. 1970) and 313 ± 10 Ma (Maluski 1972) and a U–Pb zircon age of 324 ± 5 Ma (Moussavou 1998). Finally, a post-kinematic intrusion has been dated, by Rb–Sr whole-rock isochron, at 297 ± 5 Ma (Camarat granite; Roubault *et al*. 1970).

A recent ^{40}Ar–^{39}Ar study on muscovite (Morillon *et al*. 2000) indicated the presence of two crustal blocks with distinct cooling histories on either side of the Grimaud fault, with ages being around 300 Ma in the east and 320 Ma in the west.

The Tanneron massif

No U–Pb dating results are available for granitic or metamorphic rocks of the Tanneron massif. Earlier whole-rock Rb–Sr investigations yielded an age of 397 ± 25 Ma for the migmatitic gneisses in the central part of the massif and an age of 336 ± 10 Ma for the Rouet granite (Roubault *et al*. 1970). The Rouet and Plan-de-la-Tour granites are assumed to be part of a single pluton emplaced along the Grimaud–Joyeuse fault during a late stage of dextral strike-slip motion (Onézime *et al*. 1999).

However, a recent ^{40}Ar–^{39}Ar study on muscovite (Bosse *et al*. 2003) revealed the presence of three domains with distinct cooling history: (1) the eastern Tanneron with homogeneous ages around 314 Ma, (2) the central Tanneron west of the La Moure fault with homogeneous ages around 318 Ma; (3) the western Tanneron adjacent to the Rouet magmatic complex with ages ranging from 303 to 309 Ma.

Sample description

Eight samples were collected throughout the study area for U–Pb dating on monazite, to characterize the time of high-*T* metamorphic and magmatic events. The samples are described from east to west (Fig. 2).

A sample from the eastern part of the massif was collected at La Bocca locality from a 40 cm wide and undeformed leucocratic dyke (BOC-01), which cross-cuts, at high angle, the foliation of the host migmatitic augengneiss. It consists of polygonal quartz, K-feldspar (microcline), plagioclase (Ab_{95}), millimetre- to centimetre-sized muscovite and abundant tourmaline (0.5–1 cm). Small euhedral garnet grains (0.1–0.3 mm) are also present and concentrated in muscovite-rich layers. Monazite is abundant and ranges in size from 50 to 150 μm; a few grains

Table 1. *U–Pb analytical results for monazite and initial Pb isotopic composition for cogenetic K-feldspar*

Fraction*	Weight (mg)	U (ppm)	Pb_{rad} (ppm)	$^{206}Pb/^{204}Pb$†	Rad. Pb (atomic %)‡			Atomic ratios‡						Apparent ages (Ma)		
					^{206}Pb	^{207}Pb	^{208}Pb	$^{206}Pb/^{238}U$	Error 2σ (%)	$^{207}Pb/^{235}U$	Error 2σ (%)	$^{207}Pb/^{206}Pb$	Error 2σ (%)	$^{206}Pb/^{238}U$	$^{207}Pb/^{235}U$	$^{207}Pb/^{206}Pb$
BOC-01, aplitic vein																
1, large, (2) gr, ab	0.011	6850	920	1212	31.8	1.7	66.6	0.04937	0.2	0.3546	0.3	0.05210	0.2	310.6	308.2	289.8
2, medium, (6) gr, ab	0.008	5982	984	611	26.6	1.4	72.0	0.05055	0.6	0.3656	0.6	0.05246	0.3	317.9	316.4	305.4
3, medium, (8) gr, ab	0.017	4223	949	826	19.0	1.0	80.1	0.04920	0.6	0.3533	0.7	0.05209	0.4	309.6	307.2	289.2
4, medium, (6) gr, ab	0.011	5333	988	518	23.4	1.2	75.3	0.05017	0.8	0.3662	1.6	0.05294	1.4	315.6	316.8	326.2
5, small, (14) gr, ab	0.025	6437	945	689	27.8	1.4	70.7	0.04724	0.7	0.3368	0.9	0.05172	0.2	297.6	294.8	272.8
6, small, (18) gr, ab	0.079	5978	867	2682	28.1	1.5	70.5	0.04705	0.8	0.3395	1.0	0.05234	0.08	296.4	296.8	300.4
7, small, (10) gr	0.062	3230	3258	3350	40.5	2.1	57.3	0.04730	0.9	0.3449	1.2	0.05290	0.07	297.9	300.9	324.5
8, K-fsp:§ $^{206}Pb/^{204}Pb = 18.285$; $^{207}Pb/^{204}Pb = 15.718$; $^{208}Pb/^{204}Pb = 38.481$																
TGD-01, leucogranitic vein																
9, medium, op incl, (10) gr	0.058	19918	1572	8559	52.2	2.7	45.1	0.04771	0.6	0.3454	0.6	0.05251	0.07	300.4	301.3	307.8
10, medium, (6) gr	0.028	23466	1779	5642	55.5	2.9	41.6	0.04880	0.7	0.3532	0.7	0.05249	0.08	307.2	307.1	306.6
11, large, (2) gr	0.033	37526	2258	9305	68.4	3.6	28.0	0.04780	0.9	0.3462	0.9	0.05253	0.06	301.0	301.8	308.3
12, medium, (4) gr	0.018	34619	2291	8301	64.4	3.4	32.3	0.04943	0.5	0.3578	0.5	0.05249	0.07	311.0	310.5	306.8
13, K-fsp:§ $^{206}Pb/^{204}Pb = 18.586$; $^{207}Pb/^{204}Pb = 15.888$; $^{208}Pb/^{204}Pb = 38.944$																
TGD-02, mylonitic orthogneiss																
14, medium, (13) gr	0.120	5532	971	7194	24.2	1.3	74.6	0.04903	0.6	0.3534	0.6	0.05227	0.08	308.6	307.3	297.1
15, small, op incl, (10) gr	0.094	5931	1007	5148	25.0	1.3	73.7	0.04909	0.5	0.3547	0.5	0.05239	0.07	308.9	308.2	302.6
16, medium, (7) gr	0.088	5818	1006	9836	24.8	1.3	73.9	0.04957	1.1	0.3601	1.1	0.05269	0.08	311.8	312.3	315.4
17, medium, op incl, (5) gr	0.039	5713	1062	3208	23.1	1.2	75.7	0.04965	0.4	0.3594	0.4	0.05250	0.1	312.4	311.8	307.2
18, small, op incl, (6) gr	0.026	5816	955	627	25.7	1.4	72.9	0.04879	1.0	0.3582	1.5	0.05324	1.1	307.1	310.9	339.1
19, K-fsp:§ $^{206}Pb/^{204}Pb = 19.035$; $^{207}Pb/^{204}Pb = 16.121$; $^{208}Pb/^{204}Pb = 39.311$																
TGD-05, orthogneiss																
20, small, op incl, (16) gr	0.124	5680	1130	9808	28.9	1.6	69.5	0.06659	0.7	0.5095	0.7	0.05550	0.06	415.6	418.1	432.2
21, medium, (13) gr	0.055	6299	1167	3741	30.5	1.7	67.8	0.06539	0.5	0.4955	0.5	0.05496	0.1	408.3	408.6	410.4
22, medium, (8) gr	0.049	5500	1112	1998	28.1	1.6	70.3	0.06575	0.4	0.4989	0.4	0.05503	0.09	410.5	410.9	413.2
23, small, op incl, (12) gr	0.061	4966	1060	4637	28.1	1.6	70.4	0.06922	0.5	0.5302	0.5	0.05555	0.09	431.4	431.9	434.5
24, small, (3) gr	0.009	5340	1015	1000	31.3	1.7	67.0	0.06874	0.4	0.5229	0.5	0.05517	0.2	428.6	427.1	419.1
25, small, (7) gr, ab	0.015	4056	1022	2340	24.3	1.4	74.3	0.07077	0.4	0.5443	0.5	0.05578	0.1	440.8	441.2	443.7
26, small, (8) gr, ab	0.011	4168	1265	1357	20.3	1.1	78.6	0.07126	0.3	0.5425	0.4	0.05522	0.2	443.7	440.1	421
27, small, (7) gr, ab	0.013	5692	1291	1270	25.8	1.4	72.8	0.06758	0.6	0.5113	0.6	0.05487	0.2	421.6	419.3	406.9
28, small, (11) gr, ab	0.029	1381	354	762	23.4	1.3	75.3	0.06940	0.4	0.5256	0.5	0.05493	0.2	432.6	428.9	409.3
29, K-fsp:§ $^{206}Pb/^{204}Pb = 18.217$; $^{207}Pb/^{204}Pb = 15.886$; $^{208}Pb/^{204}Pb = 38.833$																
TGD-06, leucogranite of Grime																
30, large, op incl, (2) gr	0.010	53075	2685	5683	81.6	4.3	14.1	0.04795	0.7	0.3495	0.7	0.05286	0.1	301.9	304.3	322.8
31, small, op incl, (5) gr	0.003	37028	2109	2014	77.3	4.1	18.6	0.05113	0.4	0.3748	0.5	0.05316	0.2	321.5	323.2	335.4
TGD-11, leucogranite dyke of Grime																
32, medium, (7) gr	0.028	27294	1395	3184	69.5	3.6	27.0	0.04123	0.6	0.2910	0.8	0.05120	0.05	260.4	259.4	249.7
33, medium, (12) gr	0.083	32888	1094	3724	74.5	3.8	21.7	0.02878	0.6	0.2036	0.8	0.05131	0.08	182.9	188.2	254.7
34,, medium, (6) gr	0.046	22363	1040	2946	65.4	3.3	31.3	0.03529	0.5	0.2475	0.7	0.05087	0.05	223.6	224.6	234.9
35, small, (20) gr	0.025	23123	1138	2702	66.9	3.4	29.7	0.03822	0.6	0.2665	0.8	0.05058	0.05	241.8	239.9	221.8
36, K-fsp:§ $^{206}Pb/^{204}Pb = 18.455$; $^{207}Pb/^{204}Pb = 15.886$; $^{208}Pb/^{204}Pb = 38.830$																
TGD-10, fine-grained paragneiss																
37, small, (26) gr	0.132	5372	803	7227	29.2	1.5	69.3	0.05049	0.8	0.3670	1.0	0.05272	0.1	317.6	317.4	316.6
38, large, (16) gr	0.123	5876	849	7176	30.0	1.6	68.5	0.05003	0.5	0.3635	0.4	0.05270	0.05	314.7	314.8	315.8
39, medium, (20) gr	0.137	6723	934	9109	31.4	1.7	67.0	0.05041	1.2	0.3667	1.4	0.05276	0.2	317.0	317.2	318.4
40, small, (30) gr	0.190	6745	950	6524	31.1	1.6	67.3	0.05060	0.8	0.3688	1.0	0.05286	0.1	318.2	318.8	322.8
41, K-fsp:§ $^{206}Pb/^{204}Pb = 18.183$; $^{207}Pb/^{204}Pb = 15.787$; $^{208}Pb/^{204}Pb = 38.687$																
TGD-08, Rouet granite																
42, large, op incl, (4) gr	0.072	3103	611	2274	21.2	1.1	77.7	0.04825	0.5	0.3467	0.5	0.05211	0.09	303.8	302.2	290.2
43, medium, op incl, (7) gr	0.040	6644	952	3071	28.5	1.5	70.0	0.04719	0.8	0.3373	0.8	0.05183	0.08	297.3	295.1	277.8
44, medium, op incl, (4) gr	0.050	4514	851	556	22.1	1.2	76.7	0.04812	0.5	0.3555	0.6	0.05359	0.4	302.9	308.9	353.7
45, large, op incl, (3) gr	0.011	3935	666	648	25.1	1.3	73.5	0.04914	0.4	0.3594	0.5	0.05304	0.2	309.3	311.7	330.5
46, medium, op incl, (3) gr	0.009	6398	898	1053	29.7	1.6	68.7	0.04826	0.6	0.3491	0.6	0.05246	0.2	303.8	304	305.6
47, large, (4) gr, ab	0.017	3922	758	1636	21.6	1.1	77.3	0.04825	0.3	0.3449	0.4	0.05185	0.2	303.8	300.9	278.7
48, K-fsp:§ $^{206}Pb/^{204}Pb = 18.230$; $^{207}Pb/^{204}Pb = 15.675$; $^{208}Pb/^{204}Pb = 38.614$																

*Small, grains <100 μm in length; medium, grains 100–150 μm in length; large, grains >150 μm in length; ab, air abraded; K-fsp, potassium feldspar; op incl, opaque inclusion; numbers in parentheses are numbers of grains (gr) per fraction.

†Measured ratio, corrected for mass discrimination (0.10 ± 0.05%/a.m.u.) and isotopic tracer contribution.

‡Ratio corrected for mass discrimination, isotopic tracer contribution, 60 pg of Pb blank, 1 pg of U blank, and initial common lead determined in leached K-feldspar from the same rock sample. Rad. Pb, radiogenic lead.

§Initial common Pb determined in leached K-feldspar from the same rock sample; corrected for mass discrimination (0.10 ± 0.05%/a.m.u.; Pb blank is negligible).

can reach 200 μm in length. The grains are slightly yellow, transparent to translucent, and euhedral. A sample was collected near Mandelieu from a 1 m wide leucogranitic layer (TGD-01) that is parallel to the foliation of the surrounding migmatitic gneisses. It has an isotropic porphyritic microgranular texture and is composed of quartz, feldspar (microcline), plagioclase and muscovite, with feldspar and muscovite porphyroblasts. Monazite occurs as yellow, translucent and euhedral grains; some of them contain small opaque inclusions. The grains generally range in size from 100 to 150 μm with a few larger grains up to 220 μm in length. A sample was collected from the Tanneron orthogneiss (TGD-02). This orthogneiss shows a strong mylonitic fabric and is composed of quartz, biotite, muscovite, plagioclase (oligoclase) and K-feldspar porphyroblasts, which frequently have myrmekite at the rims of the crystals. Monazite is abundant and ranges in size from 50 to 150 μm. The grains are clear, yellow, transparent and euhedral, free of inclusions or cracks.

In the central part of the massif the Bois-de-Bagnols orthogneiss (TGD-05) consists of a highly deformed granite–gneiss of granodioritic composition (Crévola & Pupin 1998). This orthogneiss is characterized by a lepidoblastic texture and is composed of elongated quartz, feldspar (microcline), plagioclase, muscovite and biotite defining the foliation planes. The monazite population consists of yellow, euhedral to subeuhedral and transparent grains, free of cracks but occasionally containing small opaque inclusions. The grains are small, varying in size from 30 to 80 μm, with slightly larger grains up to 150 μm in length. Adjacent to the Bois-de-Bagnols orthogneiss, a fine-grained migmatitic paragneiss (TGD-10) is composed of biotite, quartz and feldspar defining millimetre-scale layers. The monazite grains extracted from this sample range in size from 80 to 200 μm and are clear, sub-euhedral to anhedral, and free of cracks and inclusions. These migmatitic gneisses contain a large east–west elongated leucogranitic body (TGD-06). This leucogranite is undeformed and has a microgranular to granophyric texture. It is composed of quartz, highly altered plagioclase, K-feldspar (microcline and/or orthoclase), biotite with altered rims, muscovite, euhedral tourmaline (1–2 cm) and small garnet grains (<0.5 cm). Partial destabilization of the minerals is not associated with deformation; high static fluid activity seems to be the major factor for alteration. Monazite recovered from the main leucogranitic body (TGD-06) was rare and strongly altered. Therefore a second sample was collected within a related leucogranitic dyke (TGD-11). In both samples, monazite is dark-coloured and occurs as euhedral to anhedral crystal with strongly altered surfaces.

To the west, a sample was collected in the Rouet granite (TGD-08), which is an undeformed aluminous cordierite-bearing body (Crévola & Pupin 1994) with a porphyritic texture. This granitic body is composed of quartz, K-feldspar porphyroblasts, biotite replaced by chlorite, altered plagioclase and minor muscovite; partial alteration seems to be related to fluid circulation. This granite contains a population of euhedral, yellow and transluscent monazite grains containing usually small opaque inclusions. The monazite grains are large and range in size between 120 and 230 μm.

Geochronological results

Analytical procedure

For U–Pb dating, monazite grains were extracted from 5–10 kg of rocks, followed by conventional mineral separation (Frantz isodynamic separator®, Densitest®, heavy liquids and grain-by-grain selection under the binocular microscope). Prior to dissolution, the monazites were selected grain by grain, depending upon size and crystallographic quality. Within each sample, the most altered grains were mechanically abraded (Krogh 1982) to remove the potentially altered crystal surfaces. Monazite multigrain fractions were dissolved for 24 h in concentrated H_2SO_4 in Savilex® beakers on a hot plate at 220–230 °C (Schärer *et al*. 1990*b*). Prior to dissolution, all fractions were spiked with a mixed $^{205}Pb/^{235}U/^{233}U$ tracer, with ^{205}Pb originating from the batch produced by Parrish & Krogh (1987). Uranium and lead were separated using AG1-X8 (200–400 mesh) ion exchange resin. Element separation and purification were performed using a procedure modified after Manhès *et al*. (1978). U and Pb were loaded on the same Re single filament using silica-gel and H_3PO_4 and then ionized at 1300–1400 and 1400–1500 °C, respectively (Schärer & Gower 1988). The correction for incorporated common Pb was carried out with the isotopic compositions of Pb measured in K-feldspars extracted from the same sample as the accessory minerals (values measured are listed in Table 1). Non-altered feldspar crystals were carefully selected grain by grain under the binocular microscope, washed in 6N HCl at 120 °C for 1 h, ground in an agate mortar, and leached with a 2% HF–0.8N HBr solution for a few minutes in a ultrasonic bath (e.g. Schärer 1991) prior to dissolution in concentrated HF. All U and Pb analyses were performed at the University of Nice using a Thomson-CSF TSN 206 mass spectrometer, equipped with a single Faraday collector (axial) and a secondary electron multiplier. Mass discrimination was determined from repeated runs of the NBS-981 Pb standard and the gravimetrically calibrated $^{233}U/^{235}U$ spike, yielding $0.10 \pm 0.05\%$/a.m.u. for Pb and U. Total blanks are around 60 pg for Pb and <1 pg for U. Monazite analyses were plotted using the software Isoplot/Ex 3 (Ludwig 2003).

Representative monazite grains, covering the full range of crystallographic shape, were selected for each sample and mounted in epoxy for back-scattered electron (BSE) imaging. BSE images were obtained at the University of Mainz using a JEOL JXA-8900RL Superprobe operating at an accelerating voltage of 15 kV and a beam current of 8–12 nA. The BSE images reveal internal compositional variations that mostly reflect variation in Th and U concentrations (Stern & Sanborn 1998).

General behaviour of the U–Pb system in monazite

The results of U–Pb analyses of monazite multigrain fractions as well as the initial Pb composition of K-feldspars for each sample are given in Table 1 and corresponding concordia plots in Figures 4 and 6. The data patterns of monazite analyses show various degrees of complexity. The results plot on or slightly above the concordia. Reverse discordance of monazite data is common, and is generally explained by an excess of ^{206}Pb produced by the decay of ^{230}Th incorporated during crystallization into the monazite structure (Schärer 1984; Parrish 1990). The most accurate estimate of the U–Pb age can therefore be obtained from $^{207}Pb/^{235}U$ ratios (which are not affected by this disequilibrium). Previous studies on experimental and natural monazite demonstrate that Pb-volume diffusion is not an efficient mechanism to disturb the U–Th–Pb system within this mineral and suggest typical closure temperature >725 °C (Parrish 1990; Dahl 1997; Smith & Giletti 1997; Cherniak *et al*. 2004; Gardes *et al*. 2006). Therefore, this mineral can potentially provide time constraints on magmatic events as well as prograde to peak thermal events in high-grade metamorphic rocks. Although the U–Pb chronometer in monazite is considered as robust with respect to later high-temperature phases even under long-lasting crustal melting conditions (e.g. Parrish 1990; Schärer *et al*. 1990*a*), interpretation of U–Pb ages on monazite can be complicated by multi-stage growth (Hawkins & Bowring 1997; Baldwin *et al*. 2006; Williams *et al*. 2006) and/or alteration of the grains. The U–Pb isotopic system can be strongly influenced by fluid-driven processes and/or deformation (Teufel & Heinrich 1997; Vavra & Schaltegger 1999; Krohe & Wawrzenitz 2000; Seydoux-Guillaume *et al*. 2002) and by the presence of older inherited components (residual monazite), which may have retained an inherited lead signature through crustal melting events (Copeland *et al*. 1988; Parrish 1990; Harrison *et al*. 1995) even at temperature exceeding granulite-facies conditions (Rubatto *et al*. 2001*a*; Paquette *et al*. 2004).

U–Pb results and age interpretation

For the leucogranitic layer TGD-01 (eastern Tanneron), the BSE images reveal that crystals are mostly composed of a compositionally distinct oscillatory rim that truncates primary zoning

(Fig. 3a). The four analysed non-abraded monazite fractions define concordant results spread between 301 and 309 Ma (Fig. 4a). The fraction analyses at the lower part of the spread (fractions 9 and 11) yield within-error identical and concordant results with an average U–Pb age of 301.0 ± 1.4 Ma. At the upper end of the spread, two concordant monazite fractions (10 and 12) yield a mean $^{207}Pb/^{235}U$ age of 308.9 ± 5.2 Ma. Volume diffusion of Pb is not very common in monazite (Parrish 1990) and is considered to be extremely slow (e.g. Gardes *et al*. 2006); therefore, the younger ages could result from recrystallization, or from protracted or episodic monazite growth over 8 Ma (Foster *et al*. 2002). Therefore, the two overlapping concordant monazite fractions at the upper end of the spread are interpreted to reflect the crystallization age of the leucogranitic melt at 308.9 ± 5.2 Ma.

From the mylonitic orthogneiss TGD-02 (eastern Tanneron), five non-abraded monazite fractions were analysed (Table 1). All analyses appear isotopically homogeneous and result in a cluster of identical and concordant U–Pb ages yielding a mean $^{207}Pb/^{235}U$ age of 309.8 ± 2.2 Ma (Fig. 4b). The BSE images reveal mostly two type of grains: (1) equant grains characterized by a sector-zoned structure mostly attributed to primary magmatic growth zones (Fig. 3b); (2) grains with a more elongated shape showing a zoned core that is truncated and embayed by an irregular and dark homogeneous overgrowth (Fig. 3c). The analytical results show that both types of grains appear fairly homogeneous in U content (5530–5930 ppm; Table 1) and may reflect a mixture of high- and low-U domains. Given that the orthogneiss has undergone high-*T* dextral shearing this age may be interpreted as either the primary igneous age or the age of the ductile deformation. A complete resetting of the grain during HT shearing is unlikely, and the age of 309.8 ± 2.2 Ma is best interpreted as the time of emplacement of the granitic protolith.

From the leucogranitic dyke BOC-01 (eastern Tanneron), six of the seven monazite multigrain fractions were abraded (Table 1). The resulting data define a field of concordant or slightly reversely discordant ages (^{206}Pb excess), scattered along the concordia between 295 and 320 Ma (Fig. 4c). As three of the fractions yield identical ages at the lower end of the spread, Pb loss does not seem a plausible explanation for the spread. The upper end of the spread is defined by two abraded fractions (2 and 4) yielding within-error identical $^{207}Pb/^{235}U$ ages with an average value of 316.5 ± 1.9 Ma. Two monazite fractions (1 and 3) plot slightly above the concordia and yield a mean $^{207}Pb/^{235}U$ age of 307.7 ± 1.0 Ma. The three other fractions analysed, including the non-abraded fraction (7), define a tight cluster on or above the concordia yielding a mean $^{207}Pb/^{235}U$ age of 297.1 ± 4.9 Ma. As this dyke intrudes a migmatitic gneiss that underwent high-*T* metamorphism prior to dyke intrusion, monazite within the dyke seems to be composed of two populations: (1) grains inherited from the host-migmatitic gneiss; (2) grains newly formed in the aplitic magma. This would be consistent with the coarse-grained rims of the dyke, which suggest that the emplacement of the dyke took place in an already cool environment. In this case, the two fractions at the upper end of the spread indicate inherited grains from the host migmatitic gneiss of about 316 Ma, whereas the three fractions at the lower part of the spread are interpreted to date the solidification of this leucocratic dyke at 297.1 ± 4.9 Ma.

In the central part of the massif, the four non-abraded monazite fractions analysed from the migmatitic paragneiss (TGD-10) are identical and concordant within error and yield a average U–Pb age of 316.8 ± 1.2 Ma (Fig. 6a). The BSE images reveal that some of the monazite grains have a complex patchwork pattern (Fig. 5a) whereas others have a homogeneous internal structure (Fig. 5b). Nevertheless, the U–Pb dates indicate that the U–Pb systematics of the different chemical patterns appears homogeneous. The diffuse patchwork pattern perhaps results from solid-state recrystallization leading to a complete resetting of the U–Pb system (Zhe *et al*. 2003). The good reproducibility and concordance of the data suggest that this age is geologically meaningful. Given that this sample did not undergo a strong post-crystallization deformation, the age of 316.8 ± 1.2 Ma is best interpreted as the minimum time of

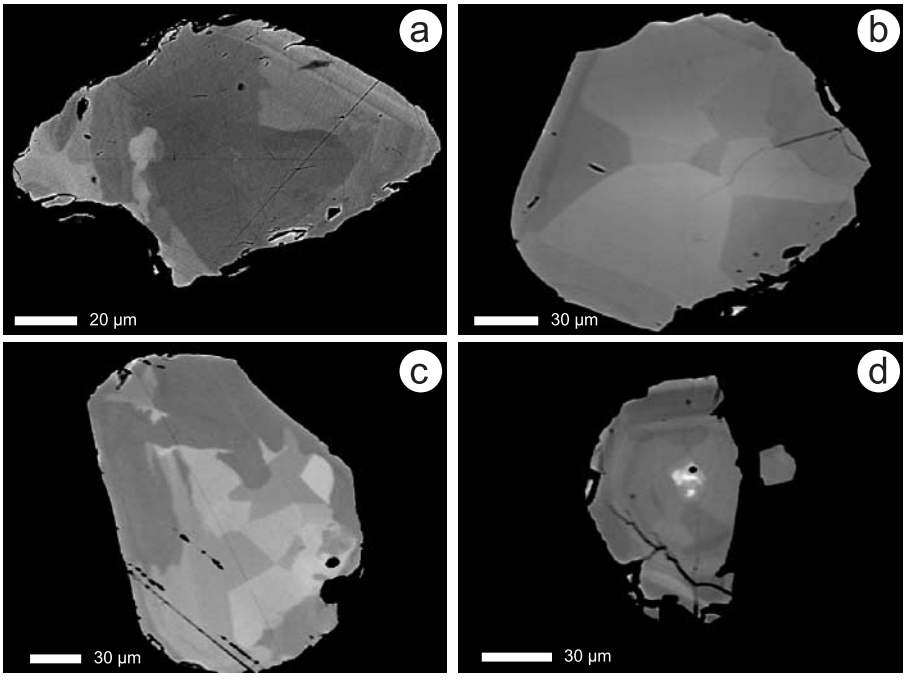

Fig. 3. Back-scattered electron (BSE) images of selected monazite grains from the leucogranitic vein TGD-01 (**a**), the mylonitic orthogneiss TGD-02 (**b**, **c**) and the leucocratic dyke BOC-01 (**d**). (**a**) Monazite grain showing a primary core cut by oscillatory compositional zoning. (**b**) Representative monazite grain displaying a sector-zoned domain and (**c**) crystal showing an embayment of a sector-zoned core domain. (**d**) Monazite grain showing sector-zoned core overgrown by an oscillatory-zoned rim.

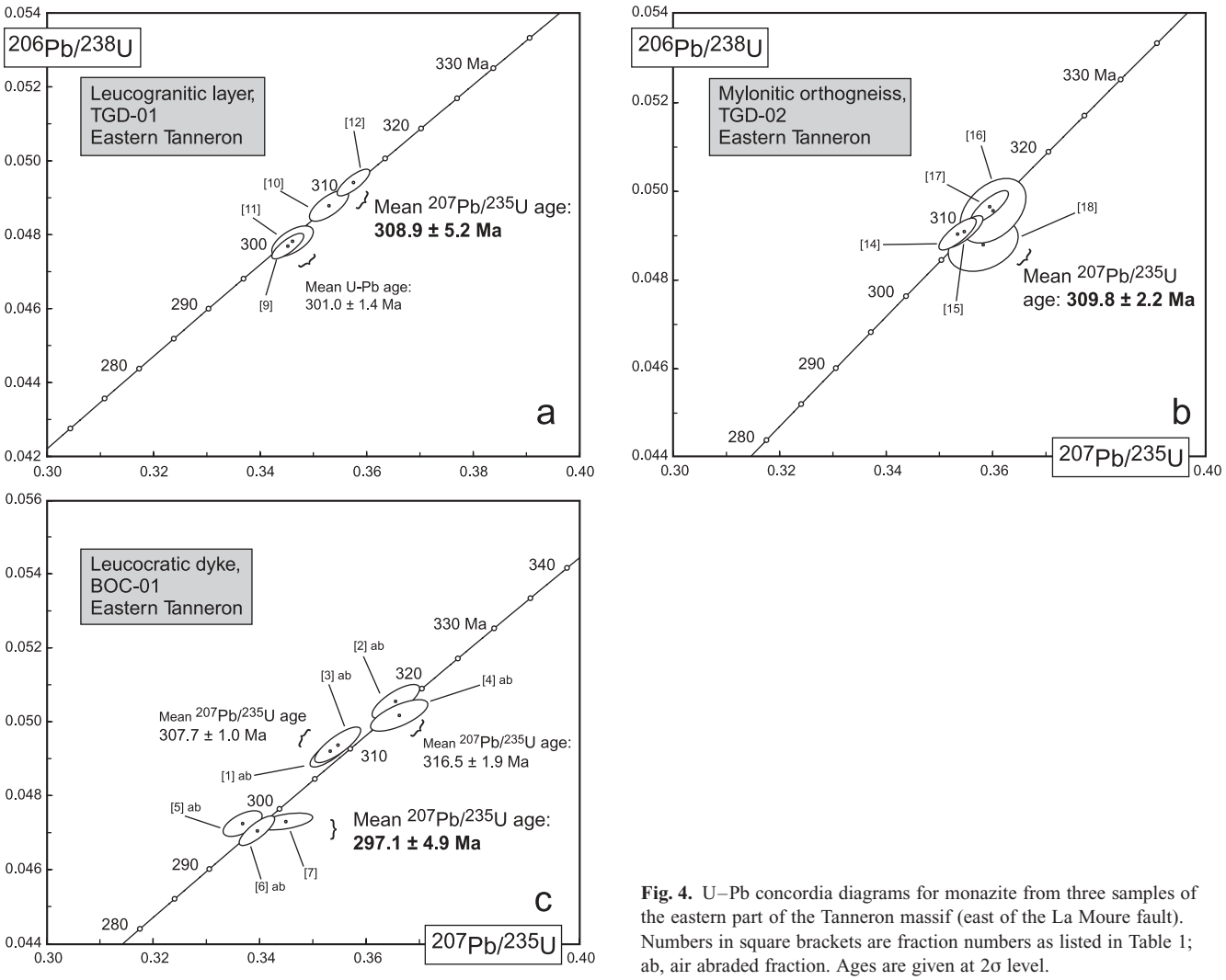

Fig. 4. U–Pb concordia diagrams for monazite from three samples of the eastern part of the Tanneron massif (east of the La Moure fault). Numbers in square brackets are fraction numbers as listed in Table 1; ab, air abraded fraction. Ages are given at 2σ level.

monazite crystallization during the last thermal peak of metamorphism in this part of the massif.

In the same area as TGD-10, no precise age can be deduced from the set of non-abraded monazite fractions analysed either from the main Grime leucogranite body (TGD-06) or from the associated leucogranitic dyke (TGD-11). The resulting data are slightly reversely discordant or normally discordant and range between 188 and 323 Ma (Fig. 6b). The high concentration of uranium (2.2–5.3%, Table 1) in these two populations makes the U–Pb isotopic system of the grains highly sensitive to late perturbation such as local late-stage fluid–mineral interaction (Seydoux-Guillaume *et al*. 2002), a feature that may partially disturb the U–Pb systematics for monazites and/or result in secondary growth domains (Townsend *et al*. 2000). As these samples show a high degree of alteration, this hypothesis seems to be the best explanation of the scatter of the data. Nevertheless, the BSE images of monazite crystals from this sample reveal that most grains are characterized by regular magmatic growth zoning (Fig. 5c). This implies that the oldest subconcordant fraction at 320 Ma may be regarded as providing an approximate emplacement age for this leucogranitic body.

For the orthogneiss TGD-05 (central Tanneron), four abraded and five non-abraded fractions were analysed (Table 1). The BSE images of monazite display complex compositional structure with generally patchy cores embayed and surrounded by compositional zoning rims with local truncations and discontinuous growth areas (Fig. 5d and e). The eight analyses result in a complex pattern (Fig. 6c) of concordant or nearly concordant (reverse or normal discordance) U–Pb data that yielded $^{207}Pb/^{235}U$ ages that span 30 Ma years, between 440.5 ± 1.3 and 409.9 ± 1.2 Ma. The spread indicates that the U–Pb isotopic system preserves a multi-stage evolution. At present it is not possible to give a single interpretation of these ages, which could reflect either the age of emplacement of the granodioritic protolith or the age of the metamorphic event that resulted in the formation of the now exposed granitic gneiss. Nevertheless, the results show that the U–Pb isotopic system in monazite was not strongly affected by the high-*T* thermal event recorded by the neighbouring migmatitic paragneisses at 317 Ma.

One abraded and five non-abraded monazite fractions were analysed from the Rouet granite TGD-08 (central Tanneron). The BSE images show for some grains complex zoned cores surrounded and dominated by thick and homogeneous rims (Fig. 5f). As suspected from the BSE images, the U–Pb system of monazites for this granite shows two discordant analyses (non-abraded fractions 44 and 45) reflecting the presence of inherited components (Fig. 6d). Three analysed fractions (two non-abraded (42 and 46) and one abraded (47)) show overlapping results that

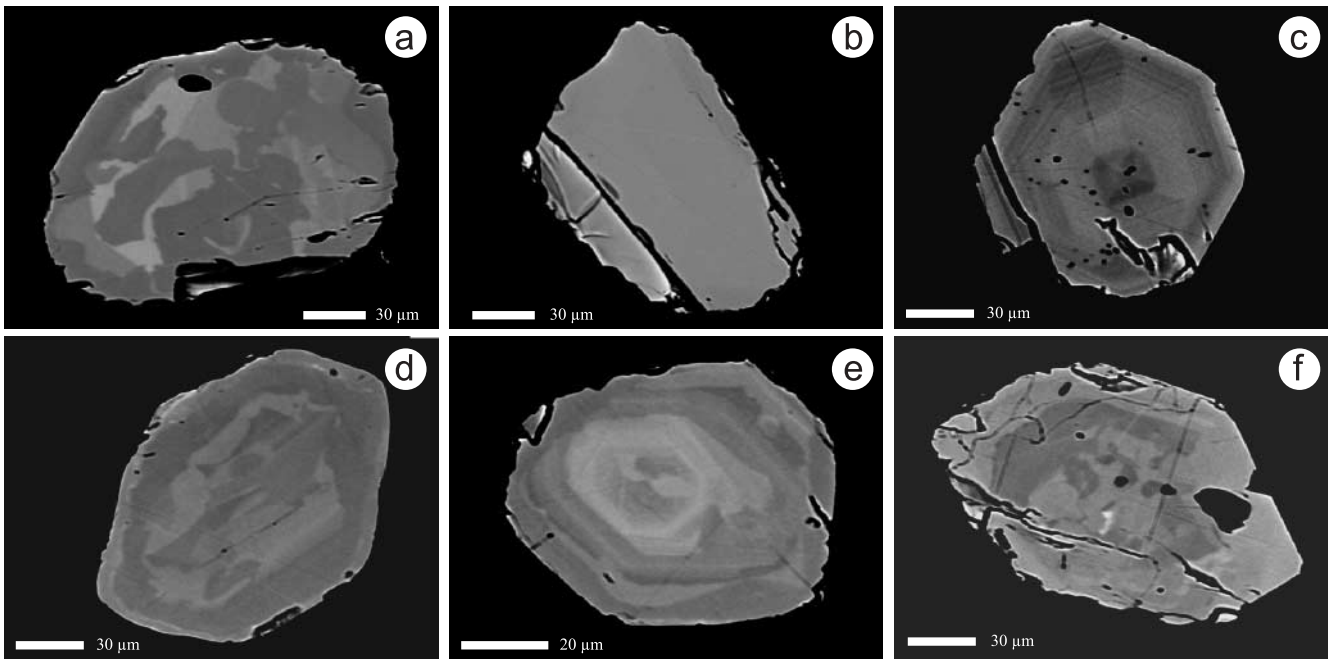

Fig. 5. BSE images of selected monazite grains from the migmatitic paragneiss TGD-10 (**a**, **b**), the leucogranitic dyke TGD-11 (**c**), the granite–gneiss TGD-05 (**d**, **e**), and the Rouet granite TGD-08 (**f**). (**a**) Metamorphic monazite showing several distinct domains with complex relationships. (**b**) Monazite with a homogeneous structure. (**c**) Representative monazite grain showing compositional oscillatory zoning. (**d**, **e**) Composite monazites, showing a core domain with large embayments (**d**), and a core domain surrounded by compositional oscillatory rims (**e**). (**f**) Monazite grain displaying a complex core domain overgrown by a homogeneous rim.

yield within error an average $^{207}Pb/^{235}U$ age of 301.8 ± 3.6 Ma, interpreted as the time of magmatic crystallization. Another non-abraded fraction (43) displays slight reverse discordance and a younger $^{207}Pb/^{235}U$ age of 295.1 ± 2.4 Ma; these features may be the result of a local late-stage hydrothermal overprint during the cooling of the granitic body.

Discussion

The results of this study show that the central part of the Tanneron massif hosts a pre-Variscan orthogneiss (TGD-05) containing monazite grains yielding ages between 440 and 410 Ma. These ages may be related to either the emplacement of the granodioritic protolith or a high-grade metamorphic event, or a combination of both. At this stage of the study, it is difficult to decipher the origin of this Silurian event. Nevertheless, it may possibly be linked to the subduction environment that existed at the Silurian active margin of Gondwana in response to the subduction of the Rheic oceanic lithosphere (Stampfli & Borel 2002; Von Raumer *et al*. 2002). This event is recorded in the neighbouring Argentera External Massif (Table 2; Paquette *et al*. 1989) and in the eastern Maures massif, where amphibolite lenses with eclogitic relicts are assumed to reflect early Silurian lithospheric subduction (Bellot 2005).

In the central part of the massif, peak-*T* metamorphic conditions are recorded at 317 ± 1 Ma by a migmatitic paragneiss (TGD-10). We consider that the generation of the Grime leucogranite (TGD-06 and TGD-11) is a large-scale end-product of this partial melting event around 317 Ma. This part of the massif underwent a subsequent rapid exhumation in the upper part of the crust, as indicated by the similar Ar–Ar ages (Bosse *et al*. 2003). This age is slightly younger than the age of the migmatization reported in the eastern Maures massif at *c*. 331 Ma (U–Pb monazite age, Moussavou 1998) and raises the question of its significance. Nevertheless, these data indicate that within the Maures–Tanneron massif, widespread crustal anatexis occurred over a time span of *c*. 14 Ma, from *c*. 331 Ma to *c*. 317 Ma. Moreover, our new monazite age of 317 ± 1 Ma is in good agreement with the timing of decompression melting dated at *c*. 317–323 Ma by U–Pb on zircon, monazite and titanite within the Argentera and External Crystalline Massifs (Table 2; Bussy *et al*. 2000; Rubatto *et al*. 2001*b*; Schaltegger *et al*. 2003).

To the east of the La Moure fault, numerous leucogranitic products crop out, and occur as asymmetrical veins either parallel or slightly oblique to the regional HT metamorphic foliation of the country gneisses. This suggests a close relation between incipient melting and HT deformation and allows us to consider these leucogranitic veins as syntectonic. This HT event is recorded at 309 ± 5 Ma by the leucogranitic veins (TGD-01), lying parallel to foliation of the country gneiss. The field observations are confirmed by the intrusion age of the Tanneron orthogneiss (TGD-02) of 310 ± 2 Ma, identical within error to the age of crystallization recorded by the synkinematic leucogranitic vein (TGD-01), and thus reflecting the same thermotectonic pulse. These results show a strong correlation between granitic intrusion, incipient melting and HT deformation, and indicate that crustal melting was still persistent at *c*. 310 Ma in the deep part of the crust. Such a Late Carboniferous magmatic pulse is well documented in the External Crystalline Massifs by the emplacement of syntectonic peraluminous granites along major-scale transcurrent faults around 307 Ma (Table 2; Schaltegger & Corfu 1992; Bussy *et al*. 2000).

In the eastern Tanneron, the U–Pb monazite data show that the leucocratic dyke BOC-01 host inherited monazites dated at

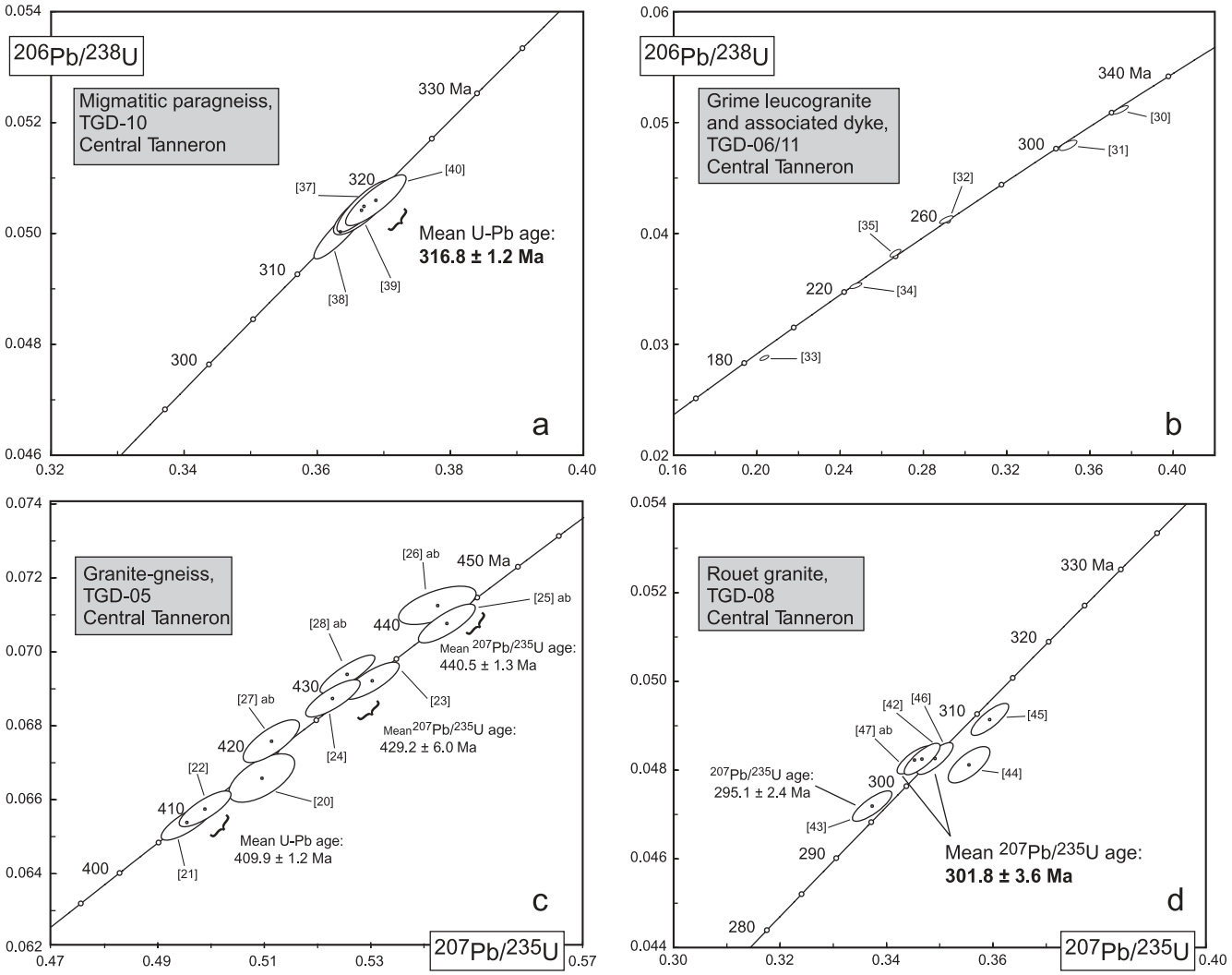

Fig. 6. U–Pb concordia diagrams for monazites from the central part of the massif (west of the La Moure fault). Numbers in square brackets are fraction numbers as listed in Table 1; ab, air abraded fraction. Ages are given at 2σ level.

316 ± 2 Ma. This age overlaps within error with the HT event recorded at 317 ± 1 Ma by the migmatitic gneiss TGD-10 from the central Tanneron, suggesting that the central and eastern parts of the Tanneron massif experienced the same Namurian HT event. However, the central Tanneron lacks the presence of the *c*. 310 Ma syntectonic granites that crop out in the eastern Tanneron (e.g. TGD-02, TGD-01). Recent Ar–Ar data (Bosse *et al*. 2003) obtained from the central and eastern Tanneron highlight distinct cooling histories for the two domains separated by the La Moure fault. Our new U–Pb data together with the previous Ar–Ar data suggest therefore that the La Moure fault played a major role during the segmentation of the massif in Late Carboniferous time. Similarities between the U–Pb and Ar–Ar ages indicate a rapid exhumation of two crustal blocks with slightly differential motion along the La Moure fault. The role of this fault is moreover indicated by the formation of the Late Carboniferous Reyran basin on its hanging wall.

Finally, in the central and eastern part of the massif, the emplacement of the Rouet granite (TGD-08) at 302 ± 4 Ma as well as the emplacement of the leucogranitic dyke (BOC-01) at 297 ± 5 Ma record a late magmatic activity. This igneous event is well correlated with post-tectonic magmatism recorded in the Maures massif by the emplacement of the undeformed Camarat granite around 300 Ma (Roubault *et al*. 1970). However, our new U–Pb monazite age of 302 ± 4 Ma on the Rouet granite is significantly younger than the intrusion age of 324 ± 5 Ma obtained by U–Pb zircon dating (Moussavou 1998) from the Plan-de-la-Tour granite in the eastern Maures. Considering the high potential of zircon grains to host inherited cores, this age of 324 ± 5 Ma might be regarded as an inherited component from the surrounding gneiss. Within the External Crystalline Massifs, post-collisional magmatism occurred between *c*. 303 and 296 Ma with the intrusion of granitic bodies such as the Mont Blanc and Aar granites (Table 2; U–Pb rutile and zircon ages, Schaltegger & Corfu 1992; U–Pb zircon ages, Bussy & von Raumer 1993).

Our new U–Pb results on the magmatism combined with Ar–Ar data from the eastern Maures (Morillon *et al*. 2000) and the Tanneron massifs (Bosse *et al*. 2003) record a thermal overprint during late orogenic extension associated with granite emplacement, rapid exhumation, and active erosion and the development of sedimentary basins in the hanging walls of brittle–ductile normal faults. In a similar way, Corsini *et al*. (2004) obtained

Table 2. *Intrusion and HT ages of Pre-Variscan and Variscan rocks dated in the Maures–Tanneron massifs, Corsica, External Crystalline Massifs and the Velay dome*

Locality	Lithology	Method	Age (Ma)	Interpretation	References
Tanneron massif	Granite–gneiss	U–Pb mon	440–410	?	This study, TGD-05
Argentera massif	Eclogite	U–Pb zr	425	HP metamorphism	Paquette *et al*. 1989
Maures massif	Amphibolite	Rb–Sr WR	348 ± 7	HT metamorphism	Innocent *et al*. 2003
Maures massif	Bormes orthogneiss	U–Pb mon	345 ± 3	HT metamorphism	Moussavou 1998
Maures massif	Migmatite	U–Pb mon	331 ± 3	HT metamorphism	Moussavou 1998
Argentera massif	Migmatite	U–Pb zr	323 ± 12	Anatexis	Rubatto *et al*. 2001*b*
Maures massif	Plan-de-la-Tour granite	Rb–Sr WR	334 ± 10	Intrusion age	Roubault *et al*. 1970
Maures massif	Plan-de-la-Tour granite	Rb–Sr WR	313 ± 10	Intrusion age	Maluski 1972
Maures massif	Plan-de-la-Tour granite	U–Pb zr	324 ± 5	Intrusion age	Moussavou 1998
Aiguilles Rouges massif	Migmatitic metagreywacke	U–Pb mon	320 ± 1	HT metamorphism	Bussy *et al*. 2000
Aiguilles Rouges massif	Metagreywacke	U–Pb mon	317 ± 2	HT metamorphism	Bussy & von Raumer 1993
Aar massif	Calc-silicate gneiss	U–Pb tit	319 ± 3	HT metamorphism	Schaltegger *et al*. 2003
Aar massif	Metapelitic layer	U–Pb mon	317 ± 2	HT metamorphism	Schaltegger *et al*. 2003
Tanneron massif	Migmatitic paragneiss	U–Pb mon	317 ± 1	HT metamorphism	This study, TGD-10
Velay dome	Migmatitic paragneiss	U–Pb mon	314 ± 5	HT metamorphism	Mougeot *et al*. 1997
Aar massif	Schöllene diorite	U–Pb rut	310 ± 3	Crystallization age	Schaltegger & Corfu 1992
Aar massif	Voralp granite	U–Pb zr	310 ± 4	Crystallization age	Schaltegger & Corfu 1992
Tanneron massif	Mylonitic orthogneiss	U–Pb mon	310 ± 2	HT deformation	This study, TGD-02
Tanneron massif	Leucogranitic layer	U–Pb mon	309 ± 5	Anatexis	This study, TGD-01
Corsica	Monzogranite	U–Pb zr	307 ± 2	Intrusion age	Paquette *et al*. 2003
Corsica	Calc-alkaline dyke	U–Pb zr	305 ± 2	Intrusion age	Paquette *et al*. 2003
Corsica	Al-rich dyke	U–Pb zr	304 ± 1	Intrusion age	Paquette *et al*. 2003
Mont Blanc massif	Mont Blanc granite	U–Pb zr	304 ± 3	Intrusion age	Bussy & von Raumer 1993
Velay dome	Biotite–cordierite granite	U–Pb mon	301 ± 5	Intrusion age	Mougeot *et al*. 1997
Tanneron massif	Rouet granite	U–Pb mon	302 ± 4	Intrusion age	This study, TGD-08
Tanneron massif	Leucogranitic dyke	U–Pb mon	297 ± 5	Intrusion age	This study, BOC-01
Maures massif	Camarat granite	Rb–Sr WR	297 ± 5	Intrusion age	Roubault *et al*. 1970
Aar massif	Aar granite	U–Pb zr	296 ± 4	Intrusion age	Schaltegger & Corfu 1992
Corsica	Gabbro–diorite	U–Pb zr	285 ± 1	Intrusion age	Paquette *et al*. 2003
Corsica	Meta-diorite	U–Pb zr	279 ± 2	Intrusion age	Paquette *et al*. 2003

mon, monazite; rut, rutile; tit, titanite; WR; whole-rock; zr, zircon.

^{40}Ar–^{39}Ar muscovite ages of 296–299 Ma from the Argentera granite located in the vicinity of the Maures–Tanneron massifs, indicative of a similar cooling history.

During Middle to Late Carboniferous times, HT–LP metamorphic conditions were widespread in the western European Variscan belt (Gardien *et al*. 1997). Crustal anatexis and intrusion of large volumes of granitic magmas were mainly related to the late phases of nappe stacking and/or to the post-collisional extensional regime that developed in response to the re-equilibration of the previously thickened crust (Faure 1995). In the eastern French Massif Central, the Velay granite–migmatite dome provides good evidence of a large crustal thermal instability that developed during the late evolution of the Variscan orogenic crust. According to Ledru *et al*. (2001), the Velay dome results from two successive phases of crustal anatexis: (1) an early stage of melting with a minimum age of 314 ± 5 Ma (Table 2; U–Pb monazite age, Mougeot *et al*. 1997); (2) a second phase of melting accompanied by large volumes of cordierite-bearing granitic magmas dated at 301 ± 5 Ma (Table 2; U–Pb monazite age, Mougeot *et al*. 1997). The temperature increase required to melt such a large volume of crust is related to several phenomena: (1) thermal relaxation and heat production of the thickened crust; (2) extra heat sources provided by underplating and intrusion of mantle-derived magmas at the base of the crust; (3) concomitant tectonic exhumation, via the activation of crustal-scale detachment faults, leading to decompression melting.

Overall, our new U–Pb monazite ages indicate that the thermal evolution of the Tanneron massif is dominated by Namurian–Stephanian HT events. As mentioned above, the timing of crustal anatexis (*c*. 317–310 Ma), which developed in response of crustal thickening and the post-collisional phase of magmatism (*c*. 303–297 Ma) associated with a local extensional regime, is in good accordance with such HT events documented in the External Crystalline Massifs and the eastern French Massif Central.

Conclusions

Our U–Pb monazite dating on metamorphic and granitic rocks in the Tanneron massif provides new time constraints on the age and duration of magmatic and metamorphic events in this area. It gives new insights into the thermotectonic evolution of this southern crystalline basement of the Variscan orogen in France. The data reveal the occurrence of three distinct high-*T* metamorphic and magmatic events from Early Silurian to Late Carboniferous–Early Permian time.

(1) Magmatism and/or high-grade metamorphism at 440–410 Ma related to a Silurian active margin setting.

(2) Variscan thermal pulses at 317–310 Ma leading to incipient anatectic melting and the emplacement of a granite-dyke complex. This event may be closely related to an active tectonic exhumation and subsequent isothermal decompression melting.

(3) Emplacement of granitic magmas at 303–297 Ma in a late to post-collisional context. Lithospheric thinning and related mantle melting seem to be required to explain these magmatic pulses.

The difference of Variscan high-*T* ages observed in the central

(317 Ma) and eastern part (310 Ma) of the massif suggests the presence of two distinct blocks. Each of them records a slightly different Variscan evolution, representing different levels of the Variscan crust. Moreover, the Tanneron massif displays a pre-Variscan and late Variscan evolution similar to that recorded in the Argentera–Mercantour massifs (Corsini *et al*. 2004), NE Sardinia–Corsica (Bellot 2005) and the External Crystalline Massifs (Schaltegger *et al*. 2003), and may therefore be related to the internal zone of the Variscan belt, as previously suggested by tectonic models (Matte 1991, 2001).

We thank U. Schaltegger for providing useful comments on an earlier draft of this manuscript. Karel Schulmann and an anonymous reviewer are thanked for their constructive reviews.

References

Baldwin, J.A., Bowring, S.A., Williams, M.L. & Mahan, K.H. 2006. U–Pb systematics in high-pressure felsic granulites from the Snowbird Tectonic Zone, Canada. *Lithos*, **88**, 173–200.

Bellot, J. 2005. The Palaeozoic evolution of the Maures massif (France) and its potential correlation with others areas of the Variscan belt: a review. *Journal of the Virtual Explorer, Electronic Edition*, **19**, Paper 4.

Bosse, V., Corsini, M. & Feraud, G. 2003. Late Variscan exhumation processes in the Tanneron massif (SE France) deduced from structural and ^{39}Ar–^{40}Ar analyses. *Geophysical Research Abstracts*, **5**, 13732.

Bouloton, J., Goncalves, P. & Pin, C. 1998. The La Croix–Valmer garnet–spinel metaperidotite (Central Maures): a cumulate of ocenic affinity involved in Early-Variscan subduction? *Comptes Rendus de l'Académie des Sciences, Série IIA*, **326**, 473–477.

Bussy, F. & von Raumer, J. 1993. U–Pb dating of Palaeozoic events in the Mont-Blanc crystalline massif, Western Alps. *Terra Abstracts*, **EGU7**, 382–383.

Bussy, F., Hernandez, J. & von Raumer, J. 2000. Bimodal magmatism as a consequence of the post-collisional readjustment of the thickened Variscan continental lithosphere (Aiguilles Rouges–Mont Blanc Massifs, Western Alps). *Transactions of the Royal Society of Edinburgh: Earth Sciences*, **91**, 221–233.

Cherniak, D.J., Watson, B.E., Harrison, M.T. & Grove, M. 2004. Pb diffusion in monazite: a combined RBS/SIMS study. *Geochimica et Cosmochimica Acta*, **68**, 829–840.

Copeland, P., Parrish, R.R. & Harrison, T.M. 1988. Identification of inherited radiogenic lead in monazite and implications for U–Pb systematics. *Nature*, **333**, 760–763.

Corsini, M., Ruffet, G. & Caby, R. 2004. Alpine and late-Hercynian geochronological constraints in the Argentera massif (Western Alps). *Eclogae Geologicae Helvetiae*, **97**, 3–15.

Crévola, G. & Pupin, J.P. 1994. Crystalline Provence: structure and Variscan evolution. *In:* Keppie, J.D. (ed.) *Pre-Mesozoic Geology in France and Related Areas*. Springer, Berlin, 426–441.

Crévola, G. & Pupin, J.P. 1998. Maures and more orthogneisses. *In: Réunion Spéciale, BRGM–SGF: Géologie du Massif des Maures, Le Plan-de-la-Tour*, 14–15.

Crévola, G., Pupin, J.P. & Toutin-Morin, N. 1991. Variscan Provence: structure and ante-Triassic geologic evolution. *In:* Piqué, A. (ed.) *Les Massifs Anciens Français*. Sciences Géologiques, **44**, 287–310.

Dahl, P.S. 1997. A crystal-chemical basis for Pb retention and fission-track annealing systematics in U-bearing minerals, with implications for geochronology. *Earth and Planetary Science Letters*, **150**, 277–290.

Faure, M. 1995. Late Carboniferous extension in the Variscan French Massif Central. *Tectonics*, **14**, 132–153.

Foster, G., Gibson, H.D., Parrish, R., Horstwood, M., Fraser, J. & Tindle, A. 2002. Textural, chemical and isotopic insights into the nature and behaviour of metamorphic monazite. *Chemical Geology*, **191**, 183–207.

Gardes, E., Jaoul, O., Montel, J.M., Seydoux-Guillaume, A.M. & Wirth, R. 2006. Pb diffusion in monazite: An experimental study of $Pb^{2+} + Th^{4+} \leftrightharpoons 2Nd^{3+}$ interdiffusion. *Geochimica et Cosmochimica Acta*, **70**, 2325–2336.

Gardien, V., Lardeaux, J.M., Ledru, P., Allemand, P. & Guillot, S. 1997. Metamorphism during late orogenic extension: insights from the French Variscan belt. *Bulletin de la Société Géologique de France*, **168**, 271–286.

Harrison, T.M., McKeegan, K.D. & LeFort, P. 1995. Detection of inherited monazite in the Manaslu leucogranite by $^{208}Pb/^{232}Th$ ion microprobe dating: Crystallization age and tectonic implications. *Earth and Planetary Science Letters*, **133**, 271–282.

Hawkins, D.P. & Bowring, S.A. 1997. U–Pb systematics of monazite and xenotime: case studies from the Paleoproterozoic of the Grand Canyon, Arizona. *Contributions to Mineralogy and Petrology*, **127**, 87–103.

Innocent, C., Michard, A., Guerrot, C. & Hamelin, B. 2003. U–Pb zircon age of 548 Ma for the leptynites (high-grade felsic rocks) of the central part of the Maures massif. Geodynamic significance of the so-called leptyno-amphibolitic complexes of the Variscan belt in western Europe. *Bulletin de la Société Géologique de France*, **174**, 585–594.

Krogh, T.E. 1982. Improved accuracy of U–Pb zircon ages by the creation of more concordant system using air abrasion technique. *Geochimica et Cosmochimica Acta*, **46**, 637–649.

Krohe, A. & Wawrzenitz, N. 2000. Domainal variations of U–Pb monazites ages and Rb–Sr whole-rock dates in polymetamorphic paragneisses (KTB Drill Core, Germany): influence of strain and deformation mechanisms on isotope systems. *Journal of Metamorphic Geology*, **18**, 271–291.

Lardeaux, J.M., Ledru, P., Daniel, I. & Duchene, S. 2001. The Variscan French Massif Central—a new addition to the ultra-high pressure metamorphic 'club': exhumation processes and geodynamic consequences. *Tectonophysics*, **332**, 143–167.

Ledru, P., Courrioux, G., Dallain, C., Lardeaux, J.M., Montel, J.M., Vanderhaeghe, O. & Vitel, G. 2001. The Velay dome (French Massif Central): melt generation and granite emplacement during orogenic evolution. *Tectonophysics*, **332**, 207–237.

Ludwig, K.R. 2003. *User's Manual for ISOPLOT/Ex 3.0. A Geochronological Toolkit for Microsoft Excel*. Berkeley Geochronology Center Special Publications, **4**.

Maluski, H. 1972. Etude $^{87}Rb/^{87}Sr$ du massif granitique du Plan-de-la-Tour (Maures). *Comptes Rendus de l'Académie des Sciences, Série IIA*, **287**, 195–198.

Maluski, H. & Allègre, C.J. 1970. Problème de la datation par le couple ^{87}Rb–^{86}Sr des socles gneissiques: exemple des gneiss de Bormes (massif hercynien des Maures, France). *Comptes Rendus de l'Académie des Sciences, Série IIA*, **270**, 18–21.

Maluski, H. & Gueirard, S. 1978. Mise en évidence par la méthode ^{40}Ar–^{39}Ar de l'âge à 580 Ma du granite de Barral (Massif des Maures, Var, France). *Comptes Rendus de l'Académie des Sciences, Série IIA*, **287**, 195–198.

Manhès, G., Minster, J.F. & Allègre, C.J. 1978. Comparative uranium–thorium–lead and rubidium–strontium study of the Saint Séverin amphoterite: consequence for early solar system chronology. *Earth and Planetary Science Letters*, **39**, 14–24.

Matte, P. 1991. Accretionary history and crustal evolution of the Variscan belt in Western Europe. *Tectonophysics*, **196**, 309–337.

Matte, P. 2001. The Variscan collage and orogeny (480–290 Ma) and the tectonic definition of the Armorica microplate: a review. *Terra Nova*, **13**, 122–128.

Morillon, A.C., Féraud, G., Sosson, M., Ruffet, G., Crévola, G. & Lerouge, G. 2000. Diachronous cooling on both sides of a major strike slip fault in the Variscan Maures Massif (South-East France), as deduced from a detailed $^{40}Ar/^{39}Ar$ study. *Tectonophysics*, **321**, 103–126.

Mougeot, R., Respaut, J.P., Ledru, P. & Marignac, C. 1997. U–Pb chronology on accessory minerals of the Velay anatectic dome (French Massif Central). *European Journal of Mineralogy*, **9**, 141–156.

Moussavou, M. 1998. *Contribution à l'histoire thermo-tectonique varisque du massif des Maures, par la typologie du zircon et la géochronologie U//Pb sur des minéraux accessoires*. PhD thesis, Montpellier University.

Onézime, J., Faure, M. & Crévola, G. 1999. Petro-structural analysis of the Rouet–Plan-de-la-Tour granitic complex (Maures and Tanneron massifs, Var, France). *Comptes Rendus de l'Académie des Sciences, Série IIA*, **328**, 773–779.

Paquette, J.L., Ménot, R.P. & Peucat, J.J. 1989. REE, Sm–Nd and U–Pb zircon study of eclogites from the Alpine External massifs (Western Alps): evidence for crustal contamination. *Earth and Planetary Science Letters*, **96**, 181–198.

Paquette, J.L., Ménot, R.P., Pin, C. & Orsini, J.B. 2003. Episodic and short-lived granitic pulse in a post-collisional setting: evidence from precise U–Pb zircon dating through a crustal cross-section in Corsica. *Chemical Geology*, **198**, 1–20.

Paquette, J.L., Goncalcves, P., Devouard, B. & Nicollet, C. 2004. Micro-drilling ID-TIMS U–Pb dating of single monazites: A new method to unravel complex poly-metamorphic evolutions. Application to the UHT granulites of Andriamena (North–Central Madagascar). *Contributions to Mineralogy and Petrology*, **147**, 110–122.

Parrish, R.R. 1990. U–Pb dating of monazite and its application to geological problems. *Canadian Journal of Earth Sciences*, **27**, 1431–1450.

Parrish, R.R. & Krogh, T.E. 1987. Synthesis and purification of ^{205}Pb for U–Pb geochronology. *Chemical Geology*, **66**, 103–110.

Roubault, M., Bordet, P., Leutwein, F., Sonet, J. & Zimmermann, J.L. 1970. Ages absolus des formations cristallophylliennes des Massifs des Maures et du Tanneron. *Comptes Rendus de l'Académie des Sciences, Série IIA*, **271**, 1067–1070.

Rubatto, D., Williams, I.S. & Buick, I.S. 2001a. Zircon and monazite response to prograde metamorphism in the Reynolds Range, Central Australia. *Contributions to Mineralogy and Petrology*, **140**, 458–468.

Rubatto, D., Schaltegger, U., Lombardo, B., Colombo, F. & Compagnoni, R. 2001b. Complex Palaeozoic magmatic and metamorphic evolution in the Argentera Massif (Western Alps) resolved with U–Pb dating. *Schweizerische Mineralogische und Petrographische Mitteilungen*, **81**, 213–228.

Schaltegger, U. & Corfu, F. 1992. The age and source for late Hercynian magmatism in the Central Alps: Evidence from precise U–Pb ages and initial Hf isotopes. *Contributions to Mineralogy and Petrology*, **111**, 329–344.

Schaltegger, U., Abrecht, J. & Corfu, F. 2003. An Ordovician orogeny in the Alpine basement: constraints from geochronology and geochemistry (Aar Massif, Central Alps). *Schweizerische Mineralogische und Petrographische Mitteilungen*, **83**, 183–195.

Schärer, U. 1984. The effect of initial ^{230}Th disequilibrium on young U–Pb ages: the Makalu case, Himalaya. *Earth and Planetary Science Letters*, **67**, 191–204.

Schärer, U. 1991. Rapid continental crust formation at 1.7 Ga from a reservoir with chondritic isotope signatures, eastern Labrador. *Earth and Planetary Science Letters*, **102**, 110–133.

Schärer, U. & Allègre, J.C. 1983. The Palung granite (Himalaya); high resolution U–Pb systematics in zircon and monazite. *Earth and Planetary Science Letters*, **63**, 423–432.

Schärer, U. & Gower, C.F. 1988. Crustal evolution in eastern Labrador: constraints from precise U–Pb ages. *Precambrian Research*, **38**, 405–421.

Schärer, U., Copeland, P., Harrison, T.M. & Searle, M.P. 1990a. Age, cooling history, and origin of post-collisional leucogranites in the Karakoram batholith; a multi-system isotope study. *Journal of Geology*, **98**, 233–251.

Schärer, U., Tapponnier, P., Lacassin, R., Leloup, P.H., Dalai, Z. & Shaosheng, J. 1990b. Intraplate tectonics in Asia: A precise age for large-scale Miocene movement along the Ailao Shan–Red River shear zone, China. *Earth and Planetary Science Letters*, **97**, 65–77.

Seydoux-Guillaume, A.M., Paquette, J.L., Wiedenbeck, M., Montel, J.M. & Heinrich, W. 2002. Experimental resetting of the U–Th–Pb systems in monazite. *Chemical Geology*, **191**, 165–181.

Seyler, M. 1982. Caractères pétrographiques et chimiques des métagabbros de la partie centrale du massif des Maures (Var). *Bulletin de la Société Géologique de France*, **24**, 717–725.

Smith, H.A. & Giletti, B.J. 1997. Lead diffusion in monazite. *Geochimica et Cosmochimica Acta*, **61**, 1047–1055.

Stampfli, G.M. & Borel, G.D. 2002. A plate tectonic model for the Paleozoic and Mesozoic constrained by dynamic plate boundaries and restored synthetic oceanic isochrons. *Earth and Planetary Science Letters*, **196**, 17–33.

Stern, R.A. & Sanborn, N. 1998. Monazite U–Pb and Th–Pb chemical geology (SHRIMP). *In: Radiogenic Age and Isotopic Studies*. Geological Survey of Canada Report, **11-1998-F**, 1–18.

Teufel, S. & Heinrich, W. 1997. Partial resetting of the U–Pb isotope system in monazite through hydrothermal experiments: a SEM and U–Pb isotope study. *Chemical Geology*, **137**, 273–281.

Toutin-Morin, N., Bonijoly, D. & Brocard, C. *et al.* 1994. *Carte géologique et notice de Fréjus–Cannes au 1/50 000ème, 2ème*. BRGM, Orléans.

Townsend, K.J., Miller, C.F., D'Andrea, J.L., Ayers, J.C., Harrison, T.M. & Coath, C.D. 2000. Low temperature replacement of monazite in the Ireteba granite, Southern Nevada: geochronological implications. *Chemical Geology*, **172**, 95–112.

Vauchez, A. & Bufalo, M. 1988. Charriage crustal, anatexie, et décrochements ductiles dans les Maures orientales (Var, France) au cours de l'orogenèse varisque. *International Journal of Earth Sciences*, **77**, 45–62.

Vavra, G. & Schaltegger, U. 1999. Post-granulite facies monazite growth and rejuvenation during Permian to Lower Jurassic thermal and fluid events in the Ivrea Zone (Southern Alps). *Contributions to Mineralogy and Petrology*, **134**, 405–414.

Von Raumer, J.F., Stampfli, G.M., Borel, G. & Bussy, F. 2002. Organization of pre-Variscan basement areas at the north-Gondwana margin. *International Journal of Earth Sciences*, **91**, 35–52.

Williams, I.S. 2001. Response of detrital zircon and monazite, and their U–Pb isotopic systems, to regional metamorphism and host-rock partial melting. *Australian Journal of Earth Sciences*, **48**, 557–580.

Williams, M.L., Jercinovic, M.J., Goncalves, P. & Mahan, K. 2006. Format and philosophy for collecting, compiling, and reporting microprobe monazite ages. *Chemical Geology*, **225**, 1–15.

Zhe, A., Williams, I.S., Brätz, H. & Millar, I.L. 2003. Different age response of zircon and monazite during the tectono-metamorphic evolution of a high grade paragneiss from the Ruhla Crystalline Complex, central Germany. *Contributions to Mineralogy and Petrology*, **145**, 691–706.

Received 13 March 2007; revised typescript accepted 2 August 2007.
Scientific editing by Alan Collins